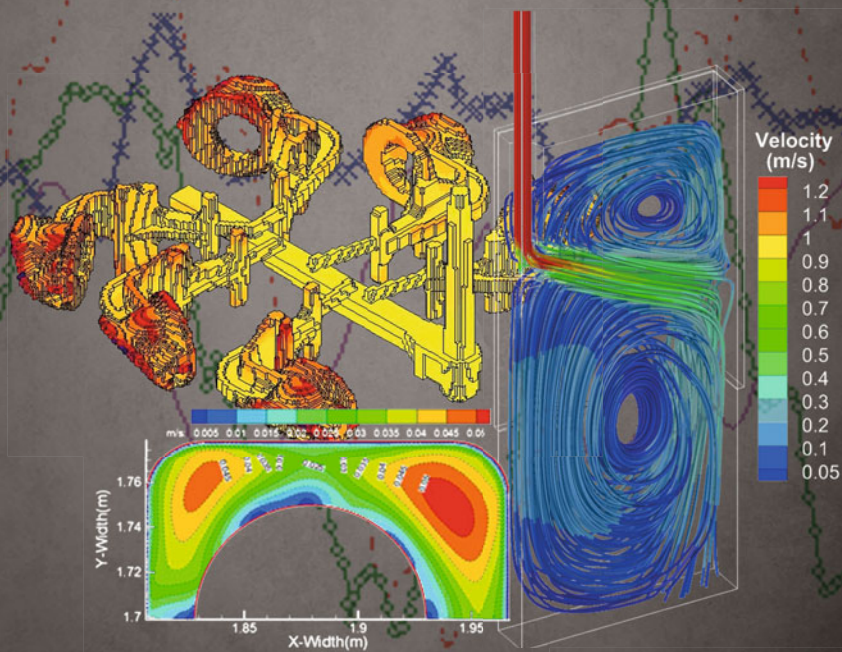# MATERIALS PROCESSING
FUNDAMENTALS 2019

Velocity (m/s)

Edited by
Guillaume Lambotte • Jonghyun Lee
Antoine Allanore • Samuel Wagstaff

TMS

Springer

The Minerals, Metals & Materials Series

Guillaume Lambotte · Jonghyun Lee ·
Antoine Allanore · Samuel Wagstaff
Editors

Materials Processing Fundamentals 2019

TMS

Springer

Editors
Guillaume Lambotte
Boston Metal
Woburn, MA, USA

Jonghyun Lee
Iowa State University
Ames, IA, USA

Antoine Allanore
Massachusetts Institute of Technology
Cambridge, MA, USA

Samuel Wagstaff
Novelis
Kennesaw, GA, USA

Cover illustration:
Bottom right: From Chapter "Effect of Casting Temperature on the Surface Finish of Grey Iron Castings", Izudin Dugic, page 93, Figure 6: 3-D temperature gradient results from the simulation when 100% of the mould is filled. https://doi.org/10.1007/978-3-030-05728-2_8
Bottom left: From Chapter "Optimization of the Flow Behavior of Molten Steel in Ultrahigh-Speed Billet Continuous Casting Mold", Pei Xu et al., page 66, Figure 6: Liquid surface velocity field of four SEN inner diameters. https://doi.org/10.1007/978-3-030-05728-2_6
Top right: From Chapter "Modeling of Steel–Slag–Air Three-Phase Flow in Continuous Casting Strand", Xubin Zhang, Wei Chen, Lifeng Zhang, Piotr Roman Scheller, page 19, Figure 3: Streamlines of liquid steel in the mold. https://doi.org/10.1007/978-3-030-05728-2_2

Preface

The symposium Materials Processing Fundamentals is hosted at the Annual Meeting of The Minerals, Metals & Materials Society (TMS) as the flagship symposium of the Process Technology and Modeling Committee. It is a unique opportunity for interdisciplinary presentations and discussions about, among others, processing, sensing, modeling, multi-physics, computational fluid dynamics, and thermodynamics.

The materials covered include ferrous and non-ferrous elements, and the processes range from mining unit operations to joining and surface finishing of materials. Acknowledging that modern processes involve multi-physics, the symposium and its proceedings allow the reader to learn the methods and outcome of other fields' modeling practices, often enabling the development of practical solutions to common problems. Modeling of basic thermodynamic and physical properties plays a key role, along with computational fluid dynamics and multi-phase transport and interface modeling.

Contributions to the proceedings include applications such as steel processing, modeling of steel and non-ferrous alloys treatments for properties control, multi-physics and computational fluid dynamics modeling for molten metal processes and properties measurement. Extractive, recovery, and recycling process modeling is also presented, completing a broad view of the field and practices of modeling in materials processing.

The engagement of TMS and committee members to chair sessions and review manuscripts makes this symposium and its proceedings possible. The editor and coeditors acknowledge the invaluable support and contribution of these volunteers as well as TMS staff members, in particular, Patricia Warren, Trudi Dunlap, and Matt Baker.

Guillaume Lambotte
Jonghyun Lee
Antoine Allanore
Samuel Wagstaff

Contents

Contents ix

About the Editors

Guillaume Lambotte is a Senior R&D Scientist at Boston Metal, a Massachusetts Institute of Technology (MIT), spin-off startup focusing on the development of an environmentally friendly and energetically efficient primary metal extraction process. He primarily focuses on computational thermodynamic modeling, electrochemistry, and high-temperature equilibrium. Prior to joining Boston Metal, he conducted research as a postdoctoral associate at the University of Massachusetts (UMass) Amherst and MIT. Before his graduate studies, he worked as a production assistant manager at Alcan Extruded Products (Crailsheim, Germany).

He obtained his bachelor degree from the European Engineer School for Materials Science (Nancy, France). He received an M.Sc. and a Ph.D. in Metallurgical Engineering from Ecole Polytechnique of Montreal (Montreal, Canada).

He is currently serving as the Chair of the TMS Process Technology and Modeling Committee and was the recipient of the 2015 TMS EPD Young Leaders Professional Development Award. In 2015, he was one of the TMS representatives at the Emerging Leaders Alliance Conference.

Jonghyun Lee is an Assistant Professor in the Department of Mechanical Engineering at Iowa State University. He has been conducting multiple industry- and government-funded projects in the field of materials processing as PI and Co-PI.

He is the recipient of the Young Leaders Professional Development Award in 2013 from The Minerals, Metals & Materials Society where he has been serving as a Co-organizer and Co-editor of the Materials Processing Fundamentals Symposium since 2014 and as Vice-Chair of the Process Modeling and Technology Committee since 2017.

Prior to joining his current institution, he was a Research Assistant Professor at the University of Massachusetts Amherst. He also had nearly 5 years of industry experience and worked as a Postdoctoral Associate for Tufts University, Medford, Massachusetts. He earned his M.S. and Ph.D. in Mechanical Engineering from the University of Massachusetts Amherst and his B.S. in the same discipline from Inha University in Incheon, South Korea.

Antoine Allanore is an Associate Professor of Metallurgy in the Department of Materials Science & Engineering at MIT. He received his higher education in Nancy (France) where he earned a chemical process engineer diploma from Ecole Nationale Supérieure des Industries Chimiques and an M.Sc. and Ph.D. from Lorraine University.

He joined MIT in 2012 as a faculty member, leading a research group that develops sustainable materials extraction and manufacturing processes. He has developed numerous alternative approaches for metals and minerals extraction and processing. With an emphasis on electrochemical methods for both analytical and processing purposes, his group combines experimental and modeling approaches to promptly investigate the ultimate state of condensed matter, the molten state. He teaches thermodynamics and sustainable chemical metallurgy at both the undergraduate and graduate levels.

He received the Vittorio de Nora Award from TMS in 2012, and the TMS Early Career Faculty Fellow Award in 2015.

Samuel Wagstaff began working in the aluminum industry at age 14 with Novelis in Spokane, Washington and now works for the same company in Kennesaw, Georgia as a Process Scientist. In 2013, he received his Bachelor of Science from Cornell University in Mechanical and Aerospace Engineering. He continued his education at the Massachusetts Institute of Technology in the Department of Materials Science and Engineering.

His Ph.D. on the minimization of macrosegregation through jet erosion of a continuously cast ingot uses a turbulent jet to reduce the uneven distribution in aluminum alloy ingots by over 70%. He finished his masters and doctorate at MIT in September 2016 after just 3 years. He has published over a dozen articles on DC casting and macrosegregation, and holds 12 patents.

Part I
Modeling of Minerals and Metals Processing

Dynamic Current and Power Distributions in a Submerged Arc Furnace

Y. A. Tesfahunegn, T. Magnusson, M. Tangstad and G. Saevarsdottir

Abstract Most submerged arc furnaces used for the production of ferroalloys run on three-phase alternating current. This affects the electrical operation of the furnace and thus it is of interest to study alternating current distributions in the system. This work presents computations of alternating electric current distributions inside an industrial submerged arc furnace for silicon production. A 3D model has been developed in ANSYS Maxwell using the eddy current solver. In each phase, electrode, central arc, crater, crater wall and side arcs that connect electrode and crater wall are taken into account. In this paper, the dynamic current distributions in different parts of the furnace, as well as skin and proximity effects in and between electrodes are presented. Moreover, active and reactive power distributions in various components of the furnace are quantified.

Keywords Current distribution · Current paths · Power distributions
Submerged arc furnace

Y. A. Tesfahunegn (✉) · G. Saevarsdottir
School of Science and Engineering, Reykjavik University, Menntavegur 1, 101, Reykjavik, Iceland
e-mail: yonatant@ru.is

G. Saevarsdottir
e-mail: gudrunsa@ru.is

T. Magnusson
United Silicon, Stakksbraut 9, 230, Reykjanesbæ, Iceland
e-mail: tm@silicon.is

M. Tangstad
Department of Materials Science and Engineering, Norwegian University of Science and Technology, 7491 Trondheim, Norway
e-mail: merete.tangstad@ntnu.no

Introduction

The current distribution in the submerged arc furnace is critical to good operation in the silicon metal production process. Phase current or resistance are among the most important control parameters, but for modern silicon metal or ferrosilicon furnaces, there is no mechanism to measure the actual current distribution. Metallurgists operate the furnaces based on the analysis of limited data at hand. Recent dig-outs of industrial furnaces have expanded available information on location-dependent charge properties, this enables more realistic modelling of electrical conditions in the furnace than previously possible. Having proper data makes the developed numerical models reliable in predicting the furnace behavior. This will enhance the understanding of critical process parameters and allow more accurate furnace control.

The current distribution is not well known for silicon furnaces and cannot be directly measured. Sævarsdottir et al. [1] calculated that the arc could be a maximum of 10–15 cm in length, based on magnetohydrodynamics (MHD) arc modelling. Although there have been publications on this subject [2], results from an accurate model where the current distribution can be calculated have not been published to date.

The geometry of the zones in a silicon furnace is dependent on the operation history, and hence a number of different geometries, sizes and compositions are possible in the various parts of the furnace. A report from recent excavations of industrial furnaces published by Tranell et al. [3] described the various zones in a FeSi furnace. Myrhaug [4] reported similar features from a pilot scale excavation operating around 150 kW. Tangstad et al. [5] published results from the excavation of industrial furnaces, where the interior of the furnace is divided into zones depending on the materials and their degree of conversion. Mapping the material distribution gives a basis for quantifying the location-dependent physical properties of the charge materials such as the electrical conductivity.

Complete numerical modeling of submerged arc furnace (SAF) requires electrical, chemical, thermal and fluid flow considerations. In this paper, we only consider the electrical aspect, which needs electrical conductivity of the different parts of the furnace. Some works have been done to address this issue. Krokstad [6] outlined an experimental method and published data on the electrical conductivity of silicon carbide and Vangskåsen [7] looked in detail at the metal producing mechanisms. Mølnås [8] and Nell and Joubert [9] have also published data on dig-out samples and material analysis that are relevant. These are some of the essential inputs necessary to set up a reasonably realistic modeling domain with correct physical properties to model the current and power distributions within a furnace, and this opens a unique opportunity to create a model which enables understanding of the current and power distributions in the furnace. These results can be used in the development of furnace control strategies that can enable improved silicon recovery and current efficiency.

The recent developments of electrical numerical modeling include several features of the furnace. Tesfahunegn et al. [10, 11] developed a 3D numerical furnace model that contains electrodes, main arcs, side arcs, crater wall, crater, and other parts

using ANSYS Fluent electric potential solver. The authors showed results for current distribution with or without taking into account the main arc. As a continuation of their work, they have implemented a vector potential method using a user-defined function in ANSYS Fluent environment to calculate dynamic current distributions [12, 13]. Their model is only able to consider electrodes and capable of predicting skin and proximity effects. Other researchers have developed different numerical models for SAF based on Computational Fluid Dynamics (CFD) and Finite Element Method (FEM). Herland et al. [14] studied proximity effects in large FeSi and FeMn furnaces using FEM. In their model, they have included different parts of the furnaces. Dhainaut [15] presented computations of electric field in SAF using CFD. The author showed the effect of contact resistance by studying the contact between two coke particles before dealing with a full-scale furnace. The furnace is partitioned in layers to consider different materials and no assumption has been made on the current path. Bezuidenhout et al. [16] applied CFD on a three-phase electric smelting furnace to investigate the electrical aspects, thermal and flow behavior. They showed relationships between electrode positions, current distribution and slag electrical resistivity. Darmana et al. [17] developed a modeling concept applicable for SAFs using CFD that considers various physical phenomena such as thermodynamics, electricity, hydrodynamics, heat radiation and chemical reactions. Wang et al. [18] investigated the thermal behavior inside three different electric furnaces for MgO production.

This paper presents computations of alternating current and power distributions inside an industrial submerged arc furnace for silicon metal production. A 3D model has been developed in ANSYS Maxwell [19] using the eddy current solver. Electrode, main arc, crater, crater wall, and side arc that connects the electrode and crater wall are taken into account for each phase. Other furnace parts such as carbon block, steel shell, and aluminum block are also incorporated.

The Process

In the silicon production process, quartz and carbon materials, that are called charge, are fed into a submerged arc furnace. Three electrodes penetrate the charge from above. Electric heating from the current provides the energy to charge through the electrodes, each of which carries one of the three phases of 50 Hz AC current, canceling out at a star point in the charge.

The overall reaction for producing Silicon metal is

$$SiO_2 + 2C = Si + 2CO(g) \tag{1}$$
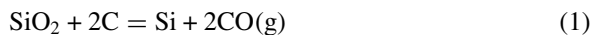
This reaction, however, takes a series of sub-reactions, changing the properties of the charge along the way as intermediary reaction products are formed. The current passes from the electrodes through the raw material charge and an electric arc burning at the tip of the electrode. The arc, which consists of thermal plasma in the range

of 10,000–20,000 K [20], provides heat for energy-consuming silicon-producing reaction (4), while the SiC-forming reaction and SiO(g) condensation reactions (2) and (3) take place at a lower temperature higher up in the furnace, see Schei et al. [21].

$$SiO(g) + 2C = SiC + CO(g) \tag{2}$$

$$2SiO(g) = Si + SiO_2 \tag{3}$$

$$SiO_2 + SiC = SiO(g) + CO(g) + Si(l) \tag{4}$$
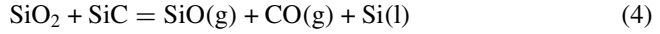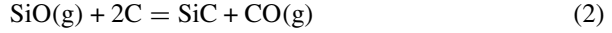
It is essential for the silicon recovery in this process that there is a balance between the high-temperature reactions (4) and the low-temperature reactions (2) and (3). Therefore, it is necessary that sufficient heat is released in the arc to drive reaction (4), while a certain part should be released in the raw material charge to drive reaction (2). The stoichiometry of reaction (4) is affected by temperature, and the ratio is decreased at higher temperature, which above 1900 °C enables a high silicon recovery. In the silicon process, it is the electric arc that creates sufficiently high temperature; therefore, sufficient arcing is important for good silicon recovery.

Computational Model

In this section, we describe the mathematical modeling, the furnace geometry, material properties, mesh generation and boundary conditions.

Mathematical Modeling

In this paper, we will focus only on the electrical aspects of SAF. The 3D electrical model is developed in ANSYS Maxwell [19] using eddy current solver, which is suitable for low-frequency devices and phenomena. It solves sinusoidally varying magnetic fields in the frequency domain. The frequency domain solution assumes frequency to be the same throughout the domain. Induced fields such as skin and current proximity effects are also considered. It is a quasi-static solver. To solve for the magnetic field $\boldsymbol{H}$, the solver computes the values as follows [19]:

$$\nabla \times \left(\frac{1}{\sigma + j\omega\varepsilon} \nabla \times \boldsymbol{H} \right) = -j\omega\mu\boldsymbol{H} \tag{5}$$

where σ, ω, μ and ε are electrical conductivity, circular frequency, magnetic permeability and electrical permittivity. The magnetic permeability is typically given by $\mu = \mu_r \mu_0$, where $\mu_0 = 4\pi \times 10^{-7}$[H/m] is the constant magnetic permeability of vacuum and μ_r [–] is the relative magnetic permeability. Once Eq. (5) is solved, the

electric field (*E*) and the electric current density (*J*) are solved using Faraday's and Ampere's laws. Also *J* and *E* are related by Ohm's law. The equation is solved using the finite element method.

Furnace Geometry and Material Properties

The computational domain is based on the actual design of a 32 MW industrial furnace with AC frequency of 50 Hz. A simplified schematic drawing of the furnace is shown in Fig. 1. The furnace is partitioned into different zones based on the material properties. Included in the modeling are the furnace lining, three electrodes, charge, molten material, three arcs below electrodes, side arcs, and three craters with crater walls made of carbides. The geometry of each electrode is considered as a truncated right conical shape. The upper surface of the electrode is the base of the cone with radius equals to the radius of the electrode. The radius of the bottom surface of the electrodes changes as the slope of the slant height changes. We assume that several concentrated side arcs are distributed around the circumference of the electrode near the tip electrodes, and the circular distances between each side arc are held constant. With this configuration, the number of side arcs increases linearly with the circumference of the electrode.

For brevity, a section of the furnace and one electrode are depicted in Fig. 1. For each phase, two types of arcs are introduced. The main-arc, burning below the electrode, with an arc length of 10 cm and diameter of 5 cm [2], and some shorter side arcs connecting the crater wall to the side of the electrode. The curvature of the three crater walls is assumed to be a circular section with a diameter of 100 cm [22]. Each
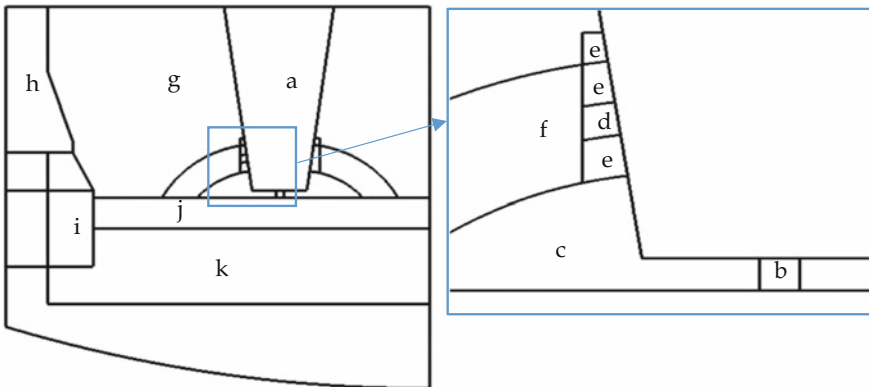
Fig. 1 Schematic of the industrial Silicon SAF with different zones (**a**) electrode, (**b**) arc, (**c**) crater, (**d**) side arc, (**e**) gap, (**f**) carbide, (**g**) charge, (**h**) alumina brick, (**i**) carbon block and carbide, (**j**) molten material, and (**k**) carbon block

Table 1 Electrical conductivity of different zones

Zones	Electrical conductivity [S/m]
Electrode [6]	225,000
Arc [22]	7000
Crater	$1e^{-14}$
Carbide [6]	400
Charge	0.15, 15
Molten material [23]	1,388,900
Carbon block [6]	225,000
Alumina brick	$1e^{-14}$
Steel shell [14]	$6.3e^{+10}$

of the zones is assumed to have constant electrical conductivity. The conductivity of each zone is taken from various literature sources and summarized in Table 1.

Mesh Generation and Boundary Conditions

Mesh generation is a crucial part of any computational method. It has a significant influence on the runtime and memory use of simulation, as well as the accuracy and stability of the solution. Since the eddy current solver utilizes an adaptive mesh refinement algorithm, the material volumes described in Section "Furnace Geometry and Material Properties" were meshed according to the method. This type of meshing technique provides automated mesh refinement capability based on reported energy error in simulation.

The model boundary conditions were imposed based on the positions of the surfaces in the model. Two types of boundary conditions are required, i.e., the natural and Neumann. The natural boundary condition is used for interface between objects. It describes the natural variation from one material to the next one, as defined by material property. The Neumann boundary condition is applied for exterior boundary of solution domain and the **H** field is tangential to the boundary and flux cannot cross it. To impose appropriate boundary conditions on the **H** field, a large far-field around the furnace which is filled with air is created. The top surface of the three electrodes is excited by current with equivalent value of $I_{rms} = 99\,kA$. The phase shift between electrodes is 120°.

Numerical Cases

In this section, we determine the current and power distributions inside the furnace described in Section "Furnace Geometry and Material Properties" as well as other parameters, such as resistance, power factor, and voltage of the system. We consider

Table 2 Two simulation groups

Category	Number of side arcs		Charge conductivity	
	8	14	0.15 S/m	15 S/m
Main arcs	✓	✓	✓	✓
No main arcs	✓	✓	✓	✓

three factors. The first factor is the number of side arcs with two levels (8 and 14), the second aspect is the charge conductivity with two levels (0.15 and 15 S/m) and the third element is the consideration of the main arcs with two levels (with main arcs and without main arcs). Hence, a total of 8 simulation cases have been performed. For discussion purposes, we group them into two categories based on the third factor. We only vary the other two factors, i.e., number of side arcs and charge conductivity. The two categories are summarized in Table 2.

For all cases, the phase current has the same value. This means that with changing domain configuration the total resistance changes, and thus the voltage for the system. Some of the cases represent realistic phase resistance in the system while others do not, and the goal with this effort is to gain a qualitative understanding of the governing mechanisms for the current and power distributions in the system. For all cases, the simulations were performed by adaptive meshing algorithm using energy error as a convergence criterion. The energy error was set to 2%. For all cases, the initial mesh size is ~$0.7e^{+06}$ elements and the simulation is converged the mesh size is ~$1.5e^{+06}$ elements. The simulation time per a case on average is around 3 h.

Since the results that are required for this study are not directly obtained from the simulation, we need to perform postprocessing. The current is calculated from current density by integrating on the surface of interest. The active power density, $p\,[W/m^3]$, given by $p = |\boldsymbol{J}|^2/2\sigma$, and the reactive power density $q\,[W/m^3]$, given by $q = (\pi f/\mu)|\boldsymbol{B}|^2$. By integrating the respective power densities over different material domain and the entire furnace, we obtain active power, $P[MW]$ and reactive power, $Q[MW]$. Once the active and reactive powers of the furnace are calculated, others results such as power factor (PF) and resistance (R) of the system can be calculated.

Figure 2 shows the resulting nonuniform current density on the three electrodes due of skin and proximity effects. Figure 3 shows the total current through electrode and the main arc at different height of the furnace. The vertical axis is a normalized current, which is the fraction of the phase current in the electrode and arc. The horizontal axis is dimensionless furnace height, which is the ratio between a given height and the total height of the furnace. In this paper, we define the total height of the furnace from the bottom of the furnace to the top of the electrodes. In Fig. 3a, main arc is considered whereas in Fig. 3b is not included. In both figures, the charge conductivity and the number of side arcs are varying as shown in Table 2. Irrespective of the magnitude of reduction, the current is decreasing from the top of the electrode to the bottom as the charge conductivity increases. Moreover, the current passed to the main-arc (Fig. 3a) is also decreased as the number of side arcs is increased.
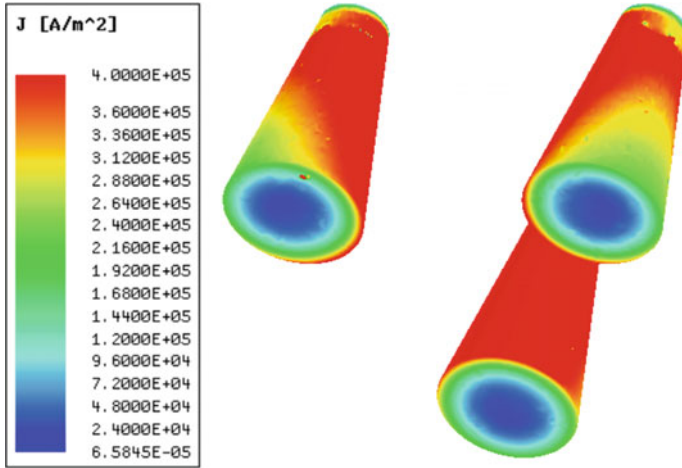
Fig. 2 Current density in the electrodes
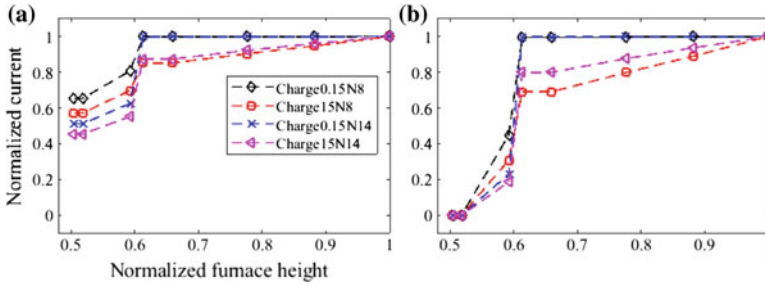
Fig. 3 Normalized current passing through electrode and main arc as a function of normalized height from the furnace bottom to the top of electrodes: (**a**) with main arc, and (**b**) without main arc

Table 3 shows the active and reactive power distributions in different zones for eight side arcs with and without main arcs consideration. Besides, the charge conductivity is varying. When the main arcs are included and charge conductivity is low, most of the power is accumulated in the main arcs and crater wall, while some power is deposited in the remaining zones. However, when the charge conductivity is changed by the order of two magnitudes, the active power in the charge is increased by the same order of magnitude while decreasing in the main arcs and crater wall. Without the main arcs, we can see the same trend except for no power in the main arcs. The main contributors to the reactive power are the far-field, charge, and electrodes. The other materials have some contributions. Since we have not included the electric components outside the furnace, such as bus bars and flexibles, the total value of the reactive power could be higher than the reported values. The simulation results for the 14 side arcs are not reported as in Table 3 since we saw the same trend. Instead, the results are summarized for all simulations results as shown in Table 4. Having

Table 3 Active and reactive power distributions in different zones for eight side arcs setup

Zones	With main arcs				No main arcs			
	Charge cond. 0.15		Charge cond. 15		Charge cond. 0.15		Charge cond. 15	
	P [MW]	Q [MW]	P [MW]	Q [MW]	P [MW]	Q [MW]	P [MW]	Q [MW]
Electrode	2.36	1.88	2.15	1.75	2.07	1.73	1.80	1.55
Main arcs	23.07	0.02	17.25	0.02	0.00	0.00	0.00	0.00
Side arcs	0.55	0.00	0.38	0.00	4.64	0.00	2.24	0.00
Crater wall	10.30	0.42	7.42	0.32	83.94	0.25	40.23	0.13
Crater	0.00	0.40	0.00	0.30	0.00	0.11	0.00	0.06
Charge	0.06	6.79	4.64	5.84	0.45	6.78	20.30	4.88
Molten Si	0.15	0.13	0.12	0.10	0.06	0.07	0.04	0.04
Carbon block	0.03	0.03	0.03	0.02	0.03	0.03	0.03	0.02
Farfield	0.00	13.00	0.00	13.00	0.00	13.00	0.00	12.99
Steel shell	0.01	0.14	0.01	0.14	0.01	0.15	0.01	0.13
Alumina brick	0.00	0.18	0.00	0.17	0.00	0.18	0.00	0.16
Total	36.53	23.00	32.00	21.66	91.18	22.29	64.63	19.97

main arcs show that resistance of the system is sensitive to the change of charge conductivity and the number of side arcs. Without the main arcs, the resistance in the furnace is increased by 100–150%, compared with corresponding simulation cases (Table 4). Most furnaces are operated to strive towards constant resistances. The variations in conductivity conditions in the furnace are met by moving the electrodes up and down. From these simulations, we see how the phase resistance can change with either the conductivity of the charge is changed and (or) exist main arcs and(or) side arcs. One of the assumptions that we made in the simulations is that for each case the charge conductivity is uniform. In a real furnace, however, the charge conductivity is increasing as it moves from the top of the furnace to the bottom. Overall the trend that can be observed is that increasing the system conductivity will result in a reduction of the system resistance.

Conclusions

This paper presents computations of dynamic current and power distributions inside an industrial submerged arc furnace for silicon production. A 3D model has been developed in ANSYS Maxwell using eddy current solver. Electrodes, main arcs, crater, crater wall, and side arcs that connect electrode and crater wall are considered

Table 4 Summary of power distributions and other results of all cases

Cases	With main arcs				No main arcs			
	P [MW]	Q [MW]	PF [/]	R [mΩ]	P [MW]	Q [MW]	PF [/]	R [mΩ]
Charge0.15_Nside8	36.53	23.00	0.85	1.24	91.18	22.29	0.97	3.10
Charge15_Nside8	32.00	21.66	0.83	1.09	64.63	19.74	0.96	2.20
Charge0.15_Nside14	29.00	21.23	0.81	0.99	51.39	20.73	0.93	1.75
Charge15_Nside14	25.77	20.37	0.78	0.78	40.19	19.50	0.9	1.37

for each phase. In this paper, the current distributions in the electrodes and main arcs and the power distributions in different parts of the furnace are presented by varying the charge conductivity, the number of side arcs and with and without main arcs. The presented model is able to capture skin and proximity effects. It was observed that the resistance of the furnace is sensitive to changes in charge conductivity, number of side arcs and existence of main arcs. When main arcs are present, most of the power is accumulated in the main arcs and crater wall for both high and low charge conductivities. It is the conductivity in the crater wall that determines the resistance in the volume at the side-arc attachment and limits the side-arc current. Thus, without main arcs, a significant portion of the power is placed in the crater and charge depending on the charge conductivity value, but the overall resistance in the system is unrealistically high. It is seen that most of the reactive power in the furnace resides in the charge and far-field and depends on the overall current in the system. It is observed that a more narrow current path tends to increase the reactive power in the furnace and thus reduce the power factor. However as the phase resistance and thus real-power dissipation is much more sensitive to the current path, the power factor is much higher for the cases without the main arcs.

References

1. Sævarsdottir GA, Bakken JA, Sevastyanenko VG, Liping Gu (2011) High power ac arcs in metallurgical furnaces. High Temp Mater Processes 15(3)
2. Saevarsdottir GA, Bakken JA (2010) Current distribution in submerged arc furnaces for silicon metal/ferrosilicon production. In: Proceedings INFACON12
3. Tranell G, Andersson M, Ringdalen E, Ostrovski O, Stenmo JJ (2010) Reaction zones in a FeSi75 furnace—results from an industrial excavation. In: INFACON XII, pp 709–715
4. Myrhaug EH (2003) Non-fossil reduction materials in the silicon process -properties and behavior. Ph.D. thesis, NTNU
5. Tangstad M, Ksiazek M, Andersen JE (2014) Zones and materials in the Si furnace. In: Proceedings: Silicon for the chemical and solar industry XII, Trondheim, Norway, June, pp 24–27
6. Krokstad M (2014) Electrical resistivity of industrial SiC crusts. M.Sc. thesis, NTNU
7. Vangskåsen J (2012) Metal-producing mechanisms in the carbothermic silicon process. M.Sc. thesis, NTNU
8. Mølnås H (2010) Investigation of SiO condensate formation in the silicon process, Project report in TMT 4500. NTNU, Norway
9. Nell J, Joubert C (2013) Phase chemistry of digout samples from a ferrosilicon furnace. In: Infacon prceedings Kazakhstan
10. Tesfahunegn YA, Magnusson T, Tangstad M, Saevarsdottir G (2018) Effect of electrode shape on the current distribution in submerged arc furnaces for silicon production—A modelling approach. J South Afr Inst Min Metall 118(6):595–600
11. Tesfahunegn, YA, Magnusson, T, Tangstad, M, Saevarsdottir, G (2018) Effect of carbide configuration on the current distribution in submerged arc furnaces for silicon production—A modelling approach. In: Nastac L, Pericleous K, Sabau A, Zhang L, Thomas B (eds) CFD modeling and simulation in materials processing 2018. TMS 2018. The Minerals, Metals & Materials Series. Springer, Cham, pp 175–185

12. Tesfahunegn, YA, Magnusson, T, Tangstad, M, Saevarsdottir, G (2018) Dynamic current distribution in the electrodes of submerged arc furnace using scalar and vector potentials. In: Shi Y et al (eds) Computational science—ICCS 2018. Lecture Notes in Computer Science, vol 10861. Springer, Cham, pp 518–527
13. Tesfahunegn, YA, Magnusson, T, Tangstad, M, Saevarsdottir, G (2018) The effect of frequency on current distributions inside submerged arc furnace. In: Paper presented at the IEEE MTT-S international conference on numerical and electromagnetic and multiphysics modeling and optimization. Reykjavik, Iceland, 08–11 Aug 2018
14. Herland EV, Sparta M, Halvorsen SA (2018) 3D models of proximity effects in large FeSi and FeMn furnaces. J South Afr Inst Min Metall 118(6):607–618
15. Dhainaut M (2004) Simulation of the electric field in a submerged arc furnace. In: INFACON X, pp 605–613
16. Bezuidenhout JJ, Eksteen JJ, Bardshaw SM (2009) Computational fluid dynamic modelling of an electric furnace used in the smelting of PGM containing concentrates. Miner Eng 22:995–1006. https://doi.org/10.1016/j.mineng.2009.03.009
17. Darmana D, Olsen JE, Tang K, Ringldalen E (2012) Modelling concept for submerged arc furnaces. In: Paper presented at the ninth international conference on CFD in the minerals and process industries CSIRO. Melbourne, Australia, 10–12 Dec
18. Wang Z, Fu Y, Wang N, Feng L (2014) 3D numerical simulation of electrical arc furnaces for the MgO production. J Mater Process Technol 214:2284–2291. https://doi.org/10.1016/j.jmatprotec.2014.04.033
19. Maxwell, ver. 18.0 (2018) ANSYS Inc., Southpointe, 275 technology drive, Canonsburg, PA 15317
20. Saevarsdottir G, Bakken J, Sevastyanenko V, Liping G (2011) High power ac arcs in metallurgical furnaces. High Temp Mater Processes 15(3)
21. Schei A, Tuset JK, Tveit H (1998) Production of high silicon alloys. Tapir Forlag, Trondheim
22. Sævarsdottir GA (2002) High current ac arcs in silicon and ferrosilicon furnaces. Ph.D. thesis, NTNU
23. Sasaki H, Ikari A, Terashima K, Kimura S (1995) Temperature dependence of the electrical resistivity of molten silicon. Jpn J Appl Phys. https://doi.org/10.1143/JJAP.34.3426

Modeling of Steel–Slag–Air Three-Phase Flow in Continuous Casting Strand

Xubin Zhang, Wei Chen, Lifeng Zhang and Piotr Roman Scheller

Abstract In the current study, a three-dimensional mold model was established by Fluent software to investigate the fluid flow of three phases (steel–slag–air) in the mold. A quarter of the mold was simulated through the k-ε model, volume of fluid (VOF) model, solidification model and continuum surface force (CFS) method. The interfacial tension between liquid steel and liquid slag and the oscillation of the mold were added into the model to show the 3D steel–slag interface. The liquid steel exiting from the submerged entry nozzle (SEN) existed as the upper backflow and lower backflow, and flowed towards the wide face and the SEN. The largest speed on the steel–slag interface was located at approximately 0.25 m from the narrow face, which was approximately 0.15 m/s. Under the influence of the upper backflow and the movement of the shell, the slag on the steel–slag interface moved from the narrow face to the SEN, and infiltrated into the gap, which affected the lubrication in the gap.

Keywords Three-phase flow · Steel–slag interface · Simulation
Continuous casting

Introduction

In the continuous casting process [1], the liquid steel in the tundish moved through the SEN into the mold [2] and then existed as double-roll flow or single-roll flow patterns [3] with different casting parameters. The powder was added into the mold successively and existed as liquid slag, solid slag and powder from the bottom up

X. Zhang · W. Chen · L. Zhang (✉) · P. R. Scheller
School of Metallurgical and Ecological Engineering, University of Science and Technology
Beijing (USTB), Beijing 100083, China
e-mail: zhanglifeng@ustb.edu.cn

X. Zhang · W. Chen · L. Zhang · P. R. Scheller
Beijing Key Laboratory of Green Recycling and Extraction of Metal,
University of Science and Technology Beijing (USTB), Beijing 100083, China

[4, 5]. The slag covering the liquid steel could protect the steel from oxidation, slow the heat transfer from the steel to the air, and absorb the inclusion from the steel. Meanwhile, the slag could infiltrate into the gap between the steel shell and the copper plate, and exist as lubricant [6], and the phenomena near the meniscus from 2D mold model [7] were shown in Fig. 1. However, the flow of the liquid steel and slag could be affected by the interaction. The slag entrapment [8] was easy to occur with the high speed of the upper backflows.

It was reported that the curved meniscus formed with the interfacial tension between the steel and slag [9]. The meniscus solidification led to the formation of hooks, which could entrap bubbles, inclusions and slags, deteriorating the surface quality of the slab [10]. Hence, the understanding of the slag movement in the mold was extremely important. However, most studies about the fluid flow in the mold only involved the flow of the steel.

In the current study, a three-dimensional mold model was established to investigate the fluid flow and heat transfer of three phases (steel–slag–air) in the mold. The double-roll flow pattern in the mold was revealed, and the velocity of the slag on the steel–slag interface and slag–air interface was obtained. The interfacial tension between liquid steel and liquid slag and the oscillation of the mold were added into the model to show the 3D steel–slag interface.
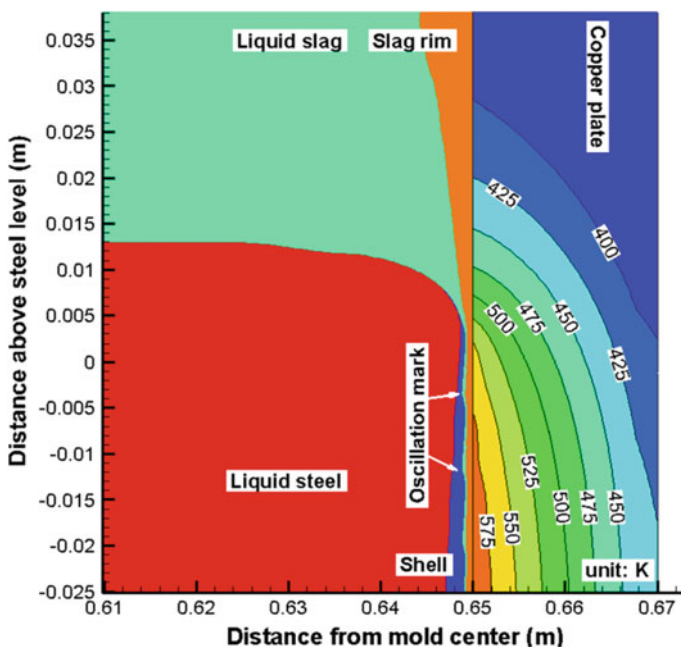

Fig. 1 Phenomena near meniscus from 2D mold model [7]

Mathematical Modeling

In the current study, a three-dimensional mathematical model was established to investigate the three-phase (Steel–slag–air) fluid flow in the mold, and the velocity on the steel–slag interface was focused on. The k-ε model, VOF (volume of fluid) model, solidification model and CFS method were applied in the model, and the fluid flow, heat transfer and the solidification of the steel were calculated through solving the continuity equation, Navier–Strokes equations, and energy equation [11]. The interfacial tension between the liquid steel and slag was considered to reveal the shape of steel–slag interface. The oscillation of the mold was added to obtain the infiltration of the slag into the gap between the steel shell and the copper plate.

The mesh and simulation conditions of the mold model are shown in Fig. 2. The computation domain included a quarter of the submerged entry nozzle (SEN), a quarter of the mold with the length of 0.9 and 0.5 m below the exit of the mold to reduce the amount of computation. In order to investigate the flow velocity near the meniscus, the finer mesh of 50 μm was applied near the initial steel–slag interface and the wall of the mold, as shown in Fig. 2(a). The total mesh number was 1462044. In Fig. 2(b), the initial thickness of the air and slag above the steel were both 50 mm. The velocity inlet (1.512 m/s) was applied at the inlet of the SEN, and the velocity was calculated on the basis of mass conservation. The temperature of the steel at the inlet was 1830 K. The pressure outlet was applied at the bottom of the model, and the turbulent kinetic energy and dissipation rate were 0.0001 m^2/s^2 and 0.0001 m^2/s^3, respectively. The free surface was applied on the top of the mold, the symmetry conditions were applied on the central section, and other boundaries were applied as non-slip wall. Simulation parameters were shown in Table 1, and other details could be found elsewhere [12]. The simulated shape of steel–slag interface was compared with the measured shape of hook lines to validate the accuracy of the model [13].

Fluid Flow in the Mold

The streamline of liquid steel in the mold is exhibited in Fig. 3. Under the current simulation condition, the liquid steel existed as double-roll flow pattern in the mold. When the liquid steel exiting from the SEN rushed to the narrow face, the liquid steel flowed towards the wide face, and then the upper and lower backflows formed. The speed of the upper and lower backflows was below 0.4 m/s. In Fig. 4, the vector of several sections in the mold is demonstrated to show the velocity of the steel and slag. Under the influence of the upper backflow, the lower part of the slag moved from the narrow face to the SEN. On the contrary, the upper part of the slag flowed from the SEN to the narrow face, when neglecting the powder slag. The speed near the steel–slag interface is larger than that near the slag–air interface. Hence, a circulation might also be found in the slag zone.

Fig. 2 Mesh and simulation conditions of the mold model

(a) Mold mesh   (b) Simulation conditions
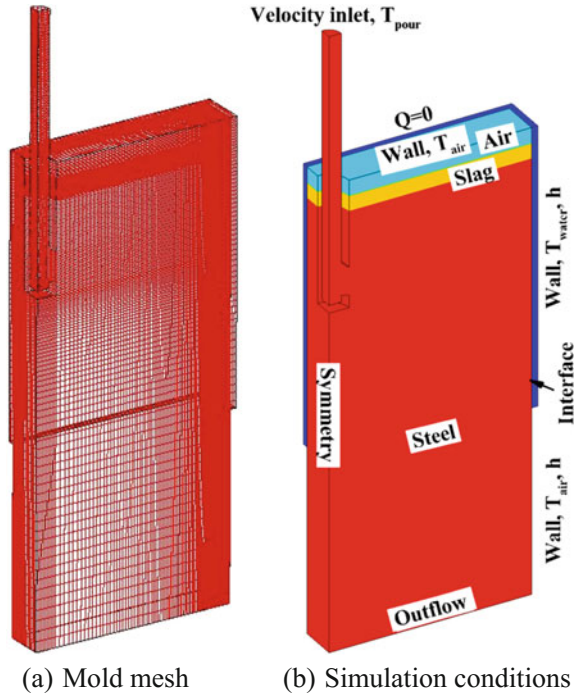
Table 1 Simulation parameters

| Parameters	Value	Parameters	Value
Mold section	1300 mm × 247 mm	Density of liquid steel	7020 kg/m^3
Simulation length	1400 mm	Viscosity of liquid steel	0.0063 kg/(m s)
Submerged depth of SEN	180 mm	Density of liquid slag	2500 kg/m^3
Inner diameter of port	85 mm	Viscosity of liquid slag	0.262 kg/(m s)
Air thickness	50 mm	Specific heat of steel	750 J/(kg K)
Slag thickness	50 mm	Latent heat of steel	270,000 J/kg
Interfacial tension of slag–steel	1.3 N/m	Mold oscillation mode	Sinusoidal
Casting speed	1.45 m/min	Oscillation frequency	3 Hz
Contact angle between steel and slag	46°	Oscillation stroke	6 mm
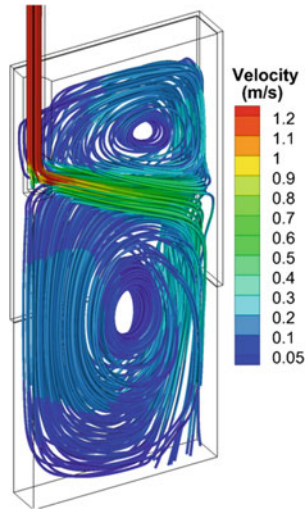
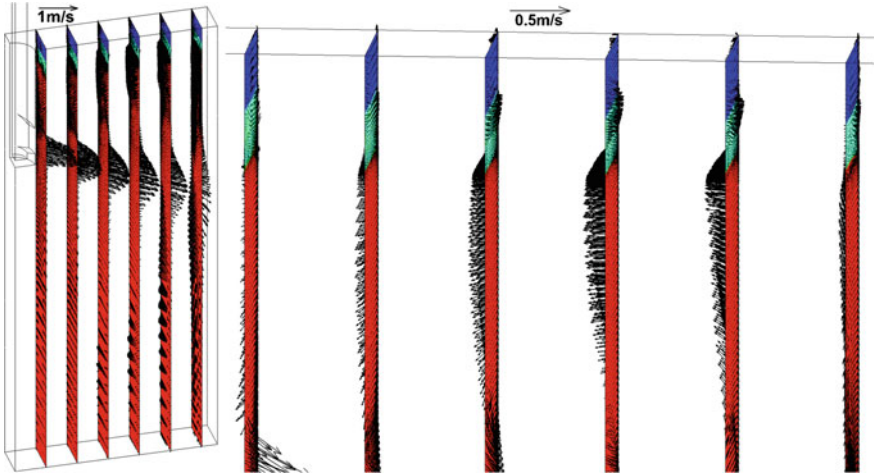**Fig. 3** Streamlines of liquid steel in the mold

Fig. 4 Vector of several sections in the mold

Velocity and Profile of the Steel–Slag Interface

In order to investigate the movement of the slag above the steel, the flow velocity on the steel–slag interface and slag–air interface is shown in Fig. 5. Under the influence of the upper backflow, the slag on the steel–slag interface flowed from the narrow face to the SEN, while the slag on the slag–air interface flowed from the SEN to the narrow face. In Fig. 5(a), the slag flowed from the point near the narrow face of the